nature communications

Article

https://doi.org/10.1038/s41467-025-61262-7

Climate–carbon-cycle interactions and spatial heterogeneity of the late Triassic Carnian pluvial episode

Received: 4 December 2024

Accepted: 17 June 2025

Published online: 30 June 2025

Check for updates

Xiangdong Zhao[1,2,10], Naihua Xue[3,4,10], Hu Yang[5,10], Daran Zheng[1], Jungang Peng[1], Joost Frieling[6], David De Vleeschouwer[4], Xuewu Fu[7], Wanglu Jia[8], Yanan Fang[1], Sha Li[1], Meng Wang[1], Xianye Zhao[3], Qiang Wang[9], Haichun Zhang[1], Jingeng Sha[1], Hugh C. Jenkyns[6], Philippe Claeys[3] & Bo Wang[1]

The Carnian Pluvial Episode (CPE; 234–232 million years ago) is an iconic but poorly understood hyperthermal event. Here, we present an integrated high-resolution (~2–10 kyr) multi-proxy record from a Carnian lacustrine succession of the Junggar Basin of northwestern China. We find that the rapid CPE onset (~15.8 kyr) could have been the result of volcanism and subsequent surface carbon-cycle feedbacks. The CPE terrestrial carbon cycling, at a scale of ±1‰ ($\delta^{13}C_{org}$), displays an in-phase relationship with the 405-kyr-long-eccentricity parameter, paralleling the warmhouse climate–carbon-cycle interactions throughout the Oligo–Miocene. The CPE hydrological cycle was typified by increased aridification in continental interiors and multiple precipitation centres at low-latitude eastern regions of Pangea and at the poles. The carbon and hydrological cycle changes of the CPE include features reminiscent of other warm events, suggesting they may share key characteristics and hold important clues to Earth system functioning.

As a typical greenhouse period in Earth's history, the Mesozoic Era was characterised by the recurrent occurrence of global hyperthermal events[1]. Investigating possible tipping points, global changes and high-resolution terrestrial responses to these Mesozoic hyperthermal events will deepen our understanding of past and present carbon-cycle perturbations. The Late Triassic Carnian Pluvial Episode or CPE (~234–232 Ma) represents a warming event characterised by oceanic anoxia[2–5] and significant enhancement of the hydrological cycle[6,7] and continental weathering[8,9]. These phenomena led to significant changes to life in marine and terrestrial ecosystems[3,10–12]. In particular, the CPE resulted in a burst of reef growth and spread of neopterygian fishes in the sea[3], as well as the radiation of terrestrial animals and plants, including dinosaurs[13,14], turtles[15], crocodiles[16], and various modern conifers[17,18]. This interval is synchronous with carbon-cycle perturbations marked by one or more pronounced global negative carbon-isotope excursions (CIEs), with amplitudes of ~2–4‰[11,19–24].

The emplacement of the Wrangellia Large Igneous Province (LIP) is considered a primary trigger of the CPE, likely amplified by the

[1]State Key Laboratory of Palaeobiology and Stratigraphy, Nanjing Institute of Geology and Palaeontology, Chinese Academy of Sciences, Nanjing, China. [2]Key Laboratory of Vertebrate Evolution and Human Origins, Institute of Vertebrate Paleontology and Paleoanthropology, Chinese Academy of Sciences, Beijing, China. [3]Archaeology, Environmental changes & Geo-Chemistry, Vrije Universiteit Brussel, Brussels, Belgium. [4]Institute of Geology and Palaeontology, University of Münster, Münster, Germany. [5]Southern Marine Science and Engineering Guangdong Laboratory (Zhuhai), Zhuhai, China. [6]Department of Earth Sciences, University of Oxford, Oxford, UK. [7]State Key Lab of Environment Geochemistry, Institute of Geochemistry, Chinese Academy of Sciences, Guiyang, China. [8]State Key Laboratory of Organic Geochemistry, Guangzhou Institute of Geochemistry, Chinese Academy of Sciences, Guangzhou, China. [9]Alfred Wegener Institute, Helmholtz Centre for Polar and Marine Research, Bremerhaven, Germany. [10]These authors contributed equally: Xiangdong Zhao, Naihua Xue, Hu Yang. e-mail: bowang@nigpas.ac.cn

release of isotopically light CO_2 from surface feedbacks into the ocean-atmosphere system, driving a warmer, more humid climate and associated negative CIEs[19,25,26]. The identification of multiple mercury (Hg) enrichments and increased input of unradiogenic osmium (Os) in sedimentary successions encompassing the CPE support a contribution from elevated volcanic emissions[26–31]. Nevertheless, the Wrangellia LIP (estimated 5×10^{18} g C)[19] alone could not have released enough isotopically light carbon to account for the magnitude (~2–4‰) of the global CIEs, as suggested by mass-balance calculations and modelling[12,19,23,32]. Consequently, despite evidence for volcanic emissions at the time of the CPE, climate-carbon cycle feedbacks may have been critical to the CPE.

The increased global humidity is widely considered a prominent feature of the CPE, supported by the record of higher terrigenous inputs into shallow-marine sediments and a shift from playa-lake and continental sabkha environments to rivers or freshwater lakes[3] (Fig. 1 and Supplementary Text 1). However, given the lack of a high-resolution chronostratigraphic framework, the correlation between enhanced humidity on land and the CPE interval remains unclear[33,34]. In several regions, including the basins of the Newark Supergroup in the USA, sedimentary evidence of increased humidity during the CPE has not been identified[35]. In addition, records of arid events have been found in the Wessex Basin (UK)[36], Central European Basin (ref. 37, but see ref. 38), and in terrigenous material (derived from aeolian dust) of a deep-sea sequence in the Inuyama area (Japan)[39] (Fig. 1 and Supplementary Text 1). Therefore, the manifestation of global hydrological cycle changes during the CPE is still under debate[33].

In this study, we report on a continuous lacustrine sequence (Dalongkou section) in the southern Junggar Basin, northwestern China, which provides a record of the CPE based on biostratigraphy and radiometric ages (radiometric methods in Supplementary Text 2) and allowed the construction of an integrated astronomically calibrated age model. The high-resolution palaeontological, sedimentological and geochemical signals from the Dalongkou section enable the detection of the CPE onset. Additionally, mercury (Hg) concentrations and isotope ratios, proxies for enhanced volcanic activity[40], have been measured within the established astronomical time frame. We further employ cyclostratigraphic and organic-carbon isotopic data to explore the carbon-cycle dynamics. Finally, we investigate the global changes in hydrological cycling during the CPE using a combination of palynological and sedimentological data, as well as Earth System modelling. Together, these data allow a comprehensive overview of climate–carbon-cycle dynamics, including potential driving mechanisms for the CPE, and coeval changes to the hydrological cycle.

Results and Discussion

Age and stratigraphy

The Junggar Basin in the Xinjiang Uygur Autonomous Region, northwestern China, is part of the Kazakhstan-Junggar Plate. The Dalongkou section (43°58′30″N, 88°53′03″E), located on the southern margin of the Junggar Basin, represents a high-palaeolatitude (~60°N) lacustrine succession that developed during the Late Triassic[41] (Fig. 1). The Huangshanjie and Karamay formations, over 500 metres thick, are continuously deposited without obvious hiatus. The Karamay Formation features significant alluvial-fan and fluvial components, with large sets of coarse sandstone and interbedded mudstone[42]. The conformably overlying Huangshanjie Formation consists largely of lacustrine deposits, dominated by dark mudstones, locally siltstone, sandstone, and interbedded limestone (Fig. 2a). Diverse plant macrofossils, spores, pollen, and vertebrate fossils in the Karamay and Huangshanjie formations attest to the lacustrine origin of these sediments[42]. The vertebrate *Fukangichthys* fauna and the palynological zonation (*Aratrisporites*, *Dictyophyllidites-Aratrisporites*, and *Lycopodiacidites-Stereisporites*) suggest that the boundary between the Middle Triassic and Upper Triassic lies between the uppermost Karamay Formation and the bottom of the Huangshanjie Formation[42]. The U-Pb radioisotopic dating on two sandstone samples from the uppermost Karamay and lower Huangshanjie layers shows a maximum depositional age of 234.8 ± 0.8 Ma to 232.9 ± 0.7 Ma (Fig. 2 and Supplementary Text 2), further constraining the lower Huangshanjie Formation to the lower–middle Carnian[43]. These absolute ages place the onset of the CPE (~234 Ma) between the Middle-Upper Triassic boundary (237 Ma) and the stratigraphic level of the sample with the youngest depositional age of 232.9 ± 0.7 Ma.

Cyclostratigraphy and chemostratigraphy

Magnetic susceptibility (MS) constitutes a sensitive proxy of lithological and environmental changes (see "Methods"). Utilising rough sedimentation rate constraints derived from age constraints (~6 cm/kyr), correlation coefficients and hypothesis testing (5- to 10-cm/kyr optimal

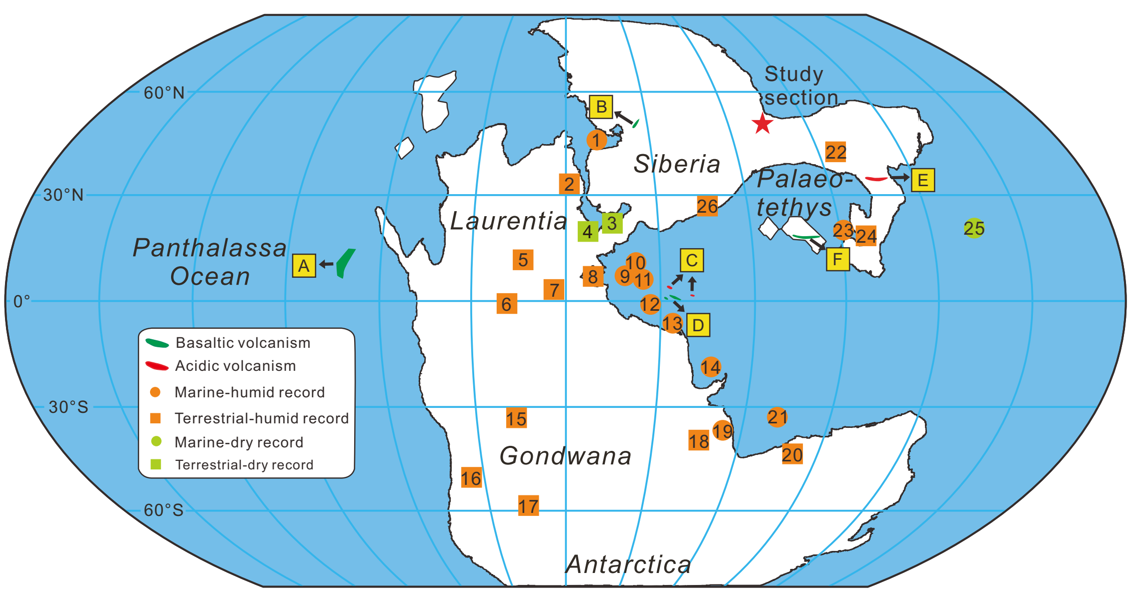

Fig. 1 | Palaeogeographical reconstruction of the Carnian world and locations of Large Igneous Provinces (LIPs) and the data indicating environmental changes during the Carnian Pluvial Episode[41]. A: Wrangellia LIP; B: South Taimyr complex; C: Kara Dere Basalt; D: Huglu-Pindos volcanic; E: Qingling-Dabie Orogenic Belt; F: Nada Kangri; detailed data on the records locations are listed in Supplementary Text 1.

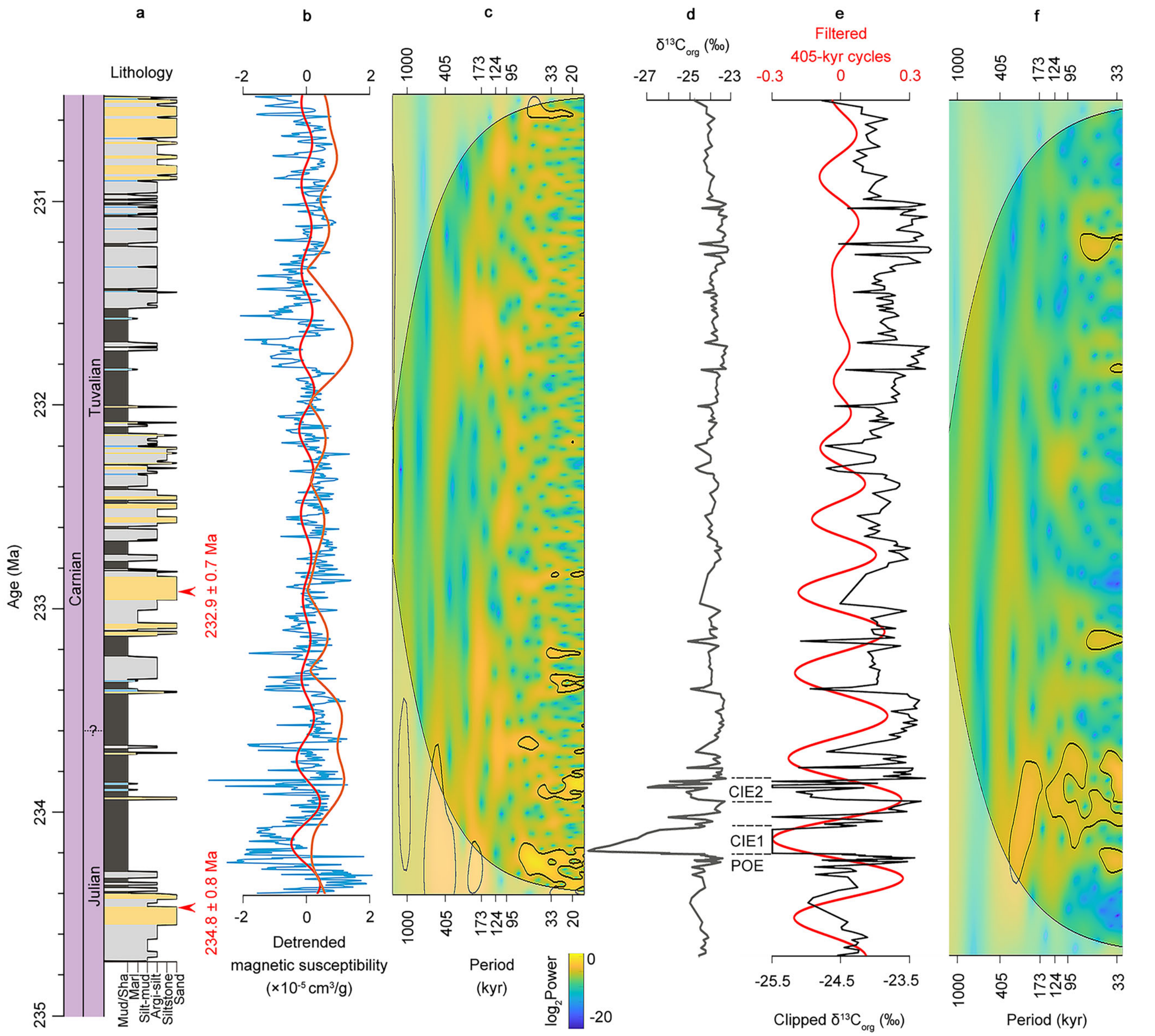

Fig. 2 | The integrated stratigraphy calibrated to the astronomical time scale of the Huangshanjie Formation, Dalongkou section (Northwest China). The lithology (**a**) is calibrated to the astronomical time scale (ATS). Detrended magnetic susceptibility (MS) series (**b**) and its Continuous Wavelet Transform (**c**). The Gaussian filtered 405-kyr long-eccentricity cycles (red curve: 0.0019–0.003 cycles/m) and amplitude modulation of the Taner filtered short-eccentricity cycles (orange curve: 0.0075–0.0115 cycles/kyr) of the detrended MS series are composited with it (**b**). **d** $\delta^{13}C_{org}$, **e** clipped $\delta^{13}C_{org}$ (from −25.5‰) is calibrated to the ATS. The red curve in (**e**) is the Gaussian filtered 405-kyr long-eccentricity cycles in clipped $\delta^{13}C_{org}$ series (0.0019–0.003 cycles/kyr). **f** continuous wavelet transform of the clipped $\delta^{13}C_{org}$ series. Abbreviations: POE, pre-onset excursion; CIE, carbon-isotope excursion; Mud, Mudstone; Sha, Shale; Silt-mud, Silty mudstone; Argi-silt, Argillaceous siltstone; Sand, Sandstone.

sedimentation rate) (Supplementary Text 3), significant Milanković cycles can be discerned through time-series analysis of the MS records in the Huangshanjie Formation (Fig. 2b, c and Supplementary Text 3). The spectral analysis of the MS series indicates a series of obvious sedimentary wavelengths, i.e., ca. 34 m, 13.3 m, 10.8 m, 9 m, 8 m, 3 m and 1.6 to 1.3 m (Supplementary Text 3), approximately in accord with the ratios of the 405-kyr long-eccentricity, 173-kyr obliquity, 125–95-kyr short-eccentricity, ~33-kyr obliquity and ~21–17-kyr precession cycles around 234 Ma, based on the La2004 astronomical solution[44]. The 405-kyr long-eccentricity and 173-kyr obliquity cycles are widely regarded as metronomes for establishment of deep-time astrochronology[45]; therefore, the inferred 405-kyr long-eccentricity (50–25 m) and 173-kyr obliquity (16.7–12.5 m) wavelengths in the MS series are tuned to the 405-kyr and 173-kyr synthetically made sinusoid, respectively. The spectral analysis of the two tuning schemes shows highly correlated astronomical signals corresponding to the 405-kyr long eccentricity, 173-kyr obliquity, and 131–95-kyr short eccentricity components, thereby confirming the reliability of the astronomical calibration (Supplementary Fig. 5). The U-Pb age of 232.9 ± 0.7 Ma was used to constrain tentatively the ~4-Myr floating astronomical time scale (ATS) tuned to the 405-kyr pure sinusoid.

We combined biostratigraphy (palynology and vertebrate fossils) and U-Pb dating to place the CPE in the lower part of the Huangshanjie Formation, and further constrained the onset of the CPE using carbon-isotope data. We present high-resolution bulk organic carbon-isotope ($\delta^{13}C_{org}$) records spanning 316.20 m, covering the top part of the Karamay Formation and the lower–middle part of the Huangshanjie Formation (~234–230 Ma, Supplementary Text 4). Our results of Rock-

https://doi.org/10.1038/s41467-025-61262-7

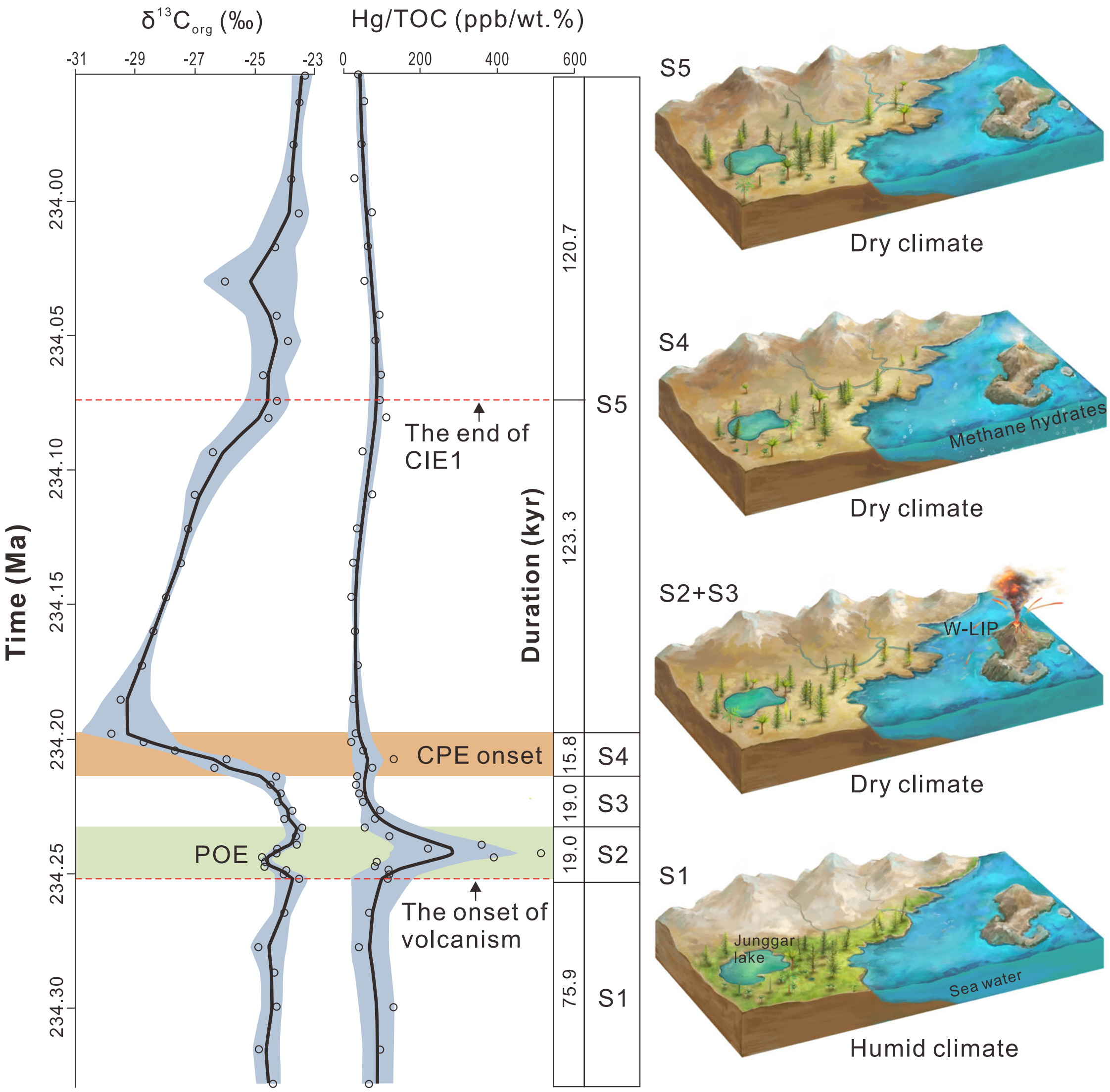

Fig. 3 | Magnification of high-resolution data of the carbon-isotope excursions (CIEs) and model for the carbon cycle during the Carnian Pluvial Episode. S1: before the Wrangellia Large Igneous Province (LIP) eruption, carbon-isotope values were stable; S2: the Wrangellia LIP began releasing isotopically light carbon, pre-onset excursion (POE) appeared, and temperatures started to rise[11]; S3: the Wrangellia LIP continued or weakened, carbon-isotope values were relatively stable, and temperatures probably continued to rise; S4: temperatures reached their peak and carbon isotopes showed an abrupt negative shift; S5: the burial of isotopically light carbon exceeded its emission, and carbon-isotope values recovered.

Eval, kerogen macerals and compound-specific (long-chain *n*-alkane) $\delta^{13}C$ analyses (analysis methods in Supplementary Text 4) indicate that the bulk organic carbon-isotope record from the Dalongkou section dominantly reflects the atmospheric $\delta^{13}C$-CO_2 signal, which reflects global carbon-cycle perturbations (Supplementary Text 4). The $\delta^{13}C_{org}$ values exhibit relatively stable background values of −25‰ to −23‰ in the basal 38.00 m, followed by pronounced (~6.5 ‰, 139.2 kyr) and moderate (~3.5‰, 114.3 kyr) negative excursions at 39.50 m to 50.50 m and 60.25 m to 71.75 m, named CIE1 and CIE2, respectively (Fig. 2d,e and Supplementary Fig. 15). Additionally, we found an abrupt but relatively weak negative $\delta^{13}C$ shift (~1.2 ‰, 19.0 kyr) stratigraphically below the level of the CPE onset (CIE 1, Fig. 3), which is here termed the pre-onset excursion (POE). A similar feature was first reported in the Palaeocene–Eocene Thermal Maximum[46] and similar phenomena were then also identified at the Triassic–Jurassic transition[47] and Cretaceous hyperthermal events (Oceanic Anoxic Event 1d[48]; Oceanic Anoxic Event 2[49]). However, there remains uncertainty as to whether the underlying mechanisms are consistent across different events, and whether they represent global phenomena. Given its short-lived duration (e.g., several centuries to many millennia in the PETM and ~19 kyr for the CPE POE here)[50], the POE may be present in other hyperthermal events but remains enigmatic as it can only be captured in those sections with sufficiently high sedimentation rate coupled with high-resolution analysis.

The two main CIEs in the Junggar Basin span about 374.2 kyr (Fig. 2 and Supplementary Fig. 15), which is broadly consistent with the time span (~300 kyr) of the first two CIEs recorded in the Bagong Formation of Tibet[31] and the Dunscombe Mudstone Formation of England[24]. However, the entire CPE with episodic CIEs is generally considered to have lasted longer than 1 Myr based on cyclostratigraphy (~1.1 Myr), biostratigraphy and magnetostratigraphy (1.6 to 1.7 Myr)[3,13,51]. We here focus on the POE and CIE1 in order to decipher the onset mechanisms behind the CPE.

Mechanistic origin of the CPE

Mercury (Hg) concentrations and isotopes have been widely used as a fingerprint of far-field volcanic activity in both marine and terrestrial settings during the extreme climatic events in the Phanerozoic Aeon (e.g., ref. 52). To explore the possible relationship between the CPE and enhanced subaerial LIP activity, high-resolution (~14-kyr average sampling interval throughout the section and ~2-kyr sampling interval near the onset of the CPE) Hg concentrations and isotopes were measured (Supplementary Text 5), and show one Hg/TOC spike in the Dalongkou section as synchronous with the POE, with elevated Hg occurring through the CIE1 (Fig. 3 and Supplementary Fig. 15). Interestingly, the Hg/TOC spike pre-dating the CIE1, little discussed in the literature, may be widespread in Europe, South China, Tibet and Japan[27,29–31], and occurs at a time of decreasing $^{187}Os/^{188}Os$ ratios recorded from far-field pelagic sections derived from the Panthalassa or palaeo-Pacific Ocean (Supplementary Fig. 16)[4,28,53].

Pre- and post- POE intervals exhibit near-zero odd-Hg MIF values (mass-independent fractionation signature, most Δ^{199}Hg values ranging from 0 to −0.04‰), whereas the POE interval itself is characterised by large ranges of odd-Hg MIF values (−0.12‰ to 0.05‰; Supplementary Fig. 15). This pattern provides evidence of a mixture of several potential sources of Hg, including terrestrial input and atmospheric deposition to the lake system during the interval of mercury enrichment[40]. The overall lower than volcanic (<0‰) range Δ^{199}Hg values indicate proportionally more terrestrial Hg (e.g., organic-rich soils with Δ^{199}Hg values of ~ −0.25‰) imported into the lacustrine system[40]. However, some high Δ^{199}Hg values also appear between the lower values, indicating that atmospheric Hg^{2+} transport (direct atmospheric deposition or photochemcial reduction of Hg^{2+}) probably contributed to the mercury enrichment, thereby offsetting the low values of the terrestrial input. In short, the results point to a volcanically derived Hg anomaly just prior to and during the CPE onset.

The coincidence of the POE and concomitant volcanically derived Hg enrichment (prior to the CIE) most likely represents a pulse of volcanism that released a relatively small mass of carbon within a short interval and caused a weak warming event (Supplementary Fig. 17)[47,48,54]. A precursor carbon release or warming event may signal the growing instability of thermally sensitive carbon sources, potentially triggering a positive feedback loop to sustain subsequent warming (Fig. 3)[50,54].

Our results show that the main carbon-isotope excursion (CIE1), which represents the CPE onset, was geologically rapid, lasting ~15.8 kyr (Fig. 3). This time interval is longer than comparable phenomena of the Triassic–Jurassic transition (1–10 kyr onset)[47] and Palaeocene-Eocene Thermal Maximum (at least 4 kyr onset)[55], but is shorter than the Permian–Triassic mass extinction (~40 kyr onset)[56], Early Jurassic T-OAE/Jenkyns Event (~65 kyr)[57], Early Cretaceous OAE1a (less than 36 kyr)[58] and the Late Cretaceous OAE 2 (~80–100 kyr)[49]. Previous geochemical modelling results suggest that the carbon released by the Wrangellia LIP alone could not have generated the magnitude of the CIE1 (~3–4‰)[20], and potential sources of additional ^{13}C-depleted carbon are hypothesised to derive from weathering of organic-rich sedimentary rocks, thawing permafrost, or dissociation of sub-ocean-floor methane hydrates[3,12,20,23]. Such potenrial additional sources of isotopically light carbon do not constitute an isolated case for the Carnian, as most carbon emission estimations from major LIPs do not match the corresponding δ^{13}C excursions (e.g., the Triassic–Jurassic transition[47] and Palaeocene-Eocene Thermal Maximum[54]). Palaeotemperature reconstructions suggest relatively warm climatic conditions before the CPE, with a global mean air temperature of ~23–24 °C[1,59] and tropical sea-surface temperatures in eastern Tethys of ~27 °C[11]. Under such warm conditions (Fig. 4a), the global permafrost surface area should be much smaller than that it is today[60]. Thus, the total amount of ^{12}C-enriched greenhouse gases from thawing permafrost is too limited to generate the magnitude of CIE1 (Supplementary Text 6). However, a hydrate reservoir only 29% the size of the modern one (>1.05×10^{19} g C)[61] could hold enough ^{13}C-depleted carbon to produce a ~3–4‰ excursion in the δ^{13}C of the exogenic carbon cycle (Supplementary Text 6). Therefore, the dissociation of sub-ocean-floor methane hydrates might be an important source of the isotopically light carbon released during the CIE1 (Fig. 3). Other feedback sources, such as peat and forest, could also contribute to the supply of ^{13}C-depleted carbon.

The sequence of events, including evidence for volcanic activity followed by a large CIE may support a scenario whereby the emplacement of the Wrangellia LIP prior to the CPE induced net positive climate–carbon-cycle feedbacks. The rapid release (~15.8 kyr) of isotopically depleted carbon from surface reservoirs such as methane hydrates could help explain the large amplitude of CIE1. Such a sequence may be consistent with strong positive feedback and potential tipping point (i.e., irreversible changes in the Earth system) behaviour during the CPE. However, we recognise that this is a simplified scenario, and the complexity of the event likely reflects multiple contributing factors. Further investigation is needed to understand fully the interplay of various processes that could have shaped the CPE.

Climate–carbon-cycle interaction through the CPE

Our results provide terrestrial insights into the climate–carbon-cycle interaction on 405-kyr long-eccentricity timescales through the CPE. Here, we use the term climate–carbon-cycle interaction to describe the coupled feedback system in which climate variables (e.g., temperature, hydrology and weathering) influence carbon-cycle processes (e.g., soil respiration, net primary productivity and CO_2 solubility), while the carbon cycle, in turn, regulates global climate by modulating atmospheric greenhouse gas concentrations (CO_2 and CH_4)[62,63]. The orbitally driven changes in Earth's hydrological processes and carbon cycles, occurring over tens of thousands to millions of years, form the underlying pattern of climate–carbon-cycle interactions[62–64]. Previous research has indicated that the climate–carbon-cycle interaction was paced by 405-kyr long-eccentricity rhythm throughout the Oligo–-Miocene time interval followed by a striking phase reversal at 6 Ma, signalling a reorganisation of the climate–carbon-cycle system in response to coldhouse conditions[63]. During eccentricity minima, cooler and more stable climates, within a generally warm background, facilitated the expansion of continental carbon reservoirs. This expansion led to greater land storage of isotopically light carbon and a corresponding rise in marine dissolved inorganic carbon (δ^{13}C-DIC), with the reverse occurring during maxima[63].

Our results reveal the pronounced in-phase variation between the filtered long-eccentricity cycles and the amplitude modulation of short eccentricity in the MS series over the CPE. This relationship suggests that the higher values of the filtered eccentricity cycles are correlated with high eccentricity (corresponding to high variance of precession), and vice versa (Fig. 2b). Remarkably, the calibrated $\delta^{13}C_{org}$ fluctuations are paced by 405-kyr long-eccentricity rhythm, on the scale of ± 1‰ (Fig. 2e, f). Therefore, the climate–carbon-cycle interaction exhibits in-phase behaviour between the terrestrial $\delta^{13}C_{org}$ series and 405-kyr long-eccentricity cycles during the CPE (Fig. 2). This in-phase behaviour is most pronounced in the CPE interval because the 405-kyr eccentricity-related forcing signal was amplified by internal climate feedbacks (e.g., enhanced seasonal differences, Supplementary Text 7) of the carbon cycle under hyperthermal conditions[62] (Supplementary Text 3).

In conclusion, our findings show that the CPE terrestrial carbon cycling, at a $\delta^{13}C_{org}$ scale of ±1‰, displays an in-phase relationship with the 405-kyr long-eccentricity metronome, which appears similar to the warmhouse climate–carbon-cycle present throughout the Oligo–Miocene interval[63]. This result, together with previous long-term carbon-isotope records[64,65], shows that such a climate–carbon-cycle interaction may have been widespread throughout the warm Mesozoic Era, including hyperthermal intervals. Therefore, this climate–carbon interaction may be the norm after the emergence of vascular plants, whereas the coldhouse climate–carbon-cycle dynamics of the earliest Pliocene may represent a more unusual situation.

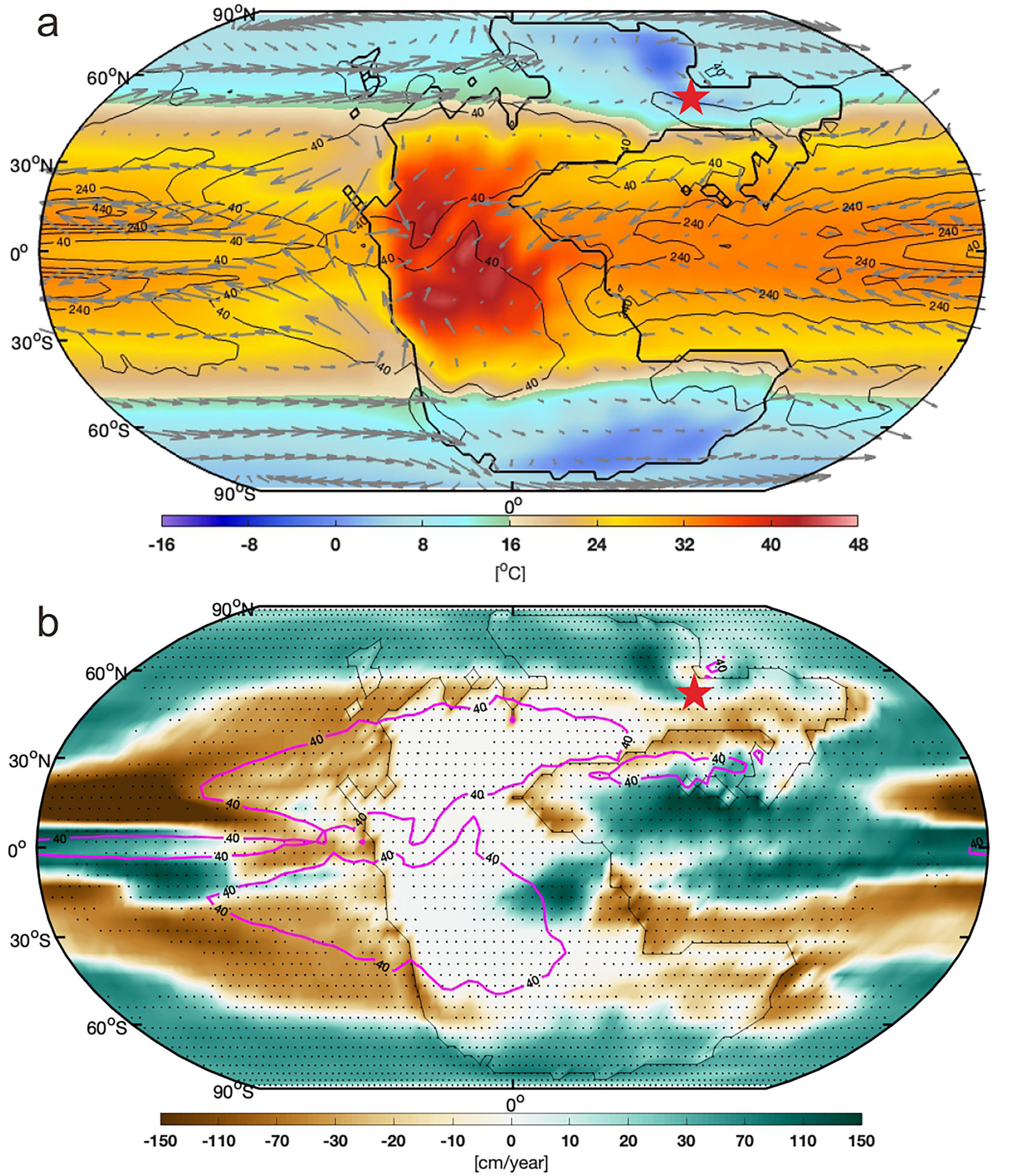

Fig. 4 | Simulated climate states before and during the Carnian Pluvial Episode (CPE). **a** Annual mean 2-m air temperature (shading), precipitation (contour, unit by cm/year) and near-surface wind before the CPE (with pCO_2 set as 568 ppmv). **b** Simulated annual mean precipitation anomalies across the CPE (pCO_2 changes from 568 ppmv to 1758 ppmv). The contours (40 cm/year) mark the arid climate zone before the CPE (low CO_2 experiment). Stippling indicates regions where the anomalies pass the 95% confidence level (Student's t-test). Our results indicate that the climate before the CPE was relatively warm with very limited coverage of permafrost. Under CO_2 forcing, the CPE climate change exhibits spatial heterogeneity in precipitation anomalies, with the expansion of the subtropical dry zone featuring reduced precipitation around the mid-latitudes. The red stars represent the location of the study section.

The hydrological cycle during the CPE

Our palynological results show an arid and warm climatic state in the Junggar Basin during the $\delta^{13}C_{org}$ fluctuations over the interval extending from the POE to the CIE2 (Supplementary Text 8 and Supplementary Fig. 15). Over this interval, the sediments exhibit a substantial decrease in hygrophytic elements (e.g., *Leiotrilete* and *Todisporites*) from averaging 22% down to ~10%. Our AWI-ESM simulations confirm a more arid and warmer climate during this interval in the Junggar Basin (Fig. 4b).

Our results show that precipitation changes during the CPE exhibited spatial heterogeneity, accompanied by a poleward shift of pre-existing precipitation zones and no evidence for global humidification. The heterogeneous pattern of precipitation changes is characterised by predominantly increased precipitation near the Equator and at high latitudes, while subtropical latitudes exhibit diminished rainfall (Fig. 4b). Moreover, mountains and extensive continental areas can block moisture transport, resulting in enhanced net evaporation within the interior of supercontinents (Pangaea)[47]. In contrast to previous hypotheses regarding unusual global humidification during the CPE[2,7,13,26], the integrated stratigraphy and Earth system model highlight the spatial variations in global precipitation patterns, characterised by increased aridification in continental interiors and the emergence of multiple precipitation centres in low-latitude eastern continents and polar regions, including the Arctic, northeastern Tethys, northeastern Gondwana, and the Antarctic (Fig. 4b). These precipitation changes are corroborated by geological records throughout the CPE (e.g. the progradation of the largest delta system in geological history in the Boreal Ocean and the westward migration of its main depocenter[66]; the large-scale increase of terrigenous inputs and the extinction of carbonate platforms in the southwestern Tethys continental shelf[67,68] and South China[11,69]) (Fig. 1). Our modelling of annual global changes, consistent with other palaeoclimatic simulations[32,70,71], is unable to replicate the wetter climate in the western and northwestern Tethys as indicated by previous sedimentological evidence (e.g., refs. 3,51). The remaining proxy–model differences may be due to unresolved local features in precipitation or the implementation of palaeotopography. Nevertheless, the newly proposed pattern appears to largely conform to established hydroclimate features observed in other past warm periods[72], thereby amplifying the spatial heterogeneity in precipitation distribution.

Implication for understanding past hyperthermal events

Understanding climate–carbon-cycle interactions and tempo of past hyperthermal events is essential to accurately project the consequences of anthropogenic carbon emissions. Our findings suggest that the CPE shares key features and perhaps driving mechanisms with several other hyperthermal events including the Triassic–Jurassic hyperthermal event, Cretaceous OAEs, as well as the Palaeocene–Eocene Thermal Maximum. Although these hyperthermal events commonly lasted up to a few million years, the onset of each appears geologically rapid, lasting 1–20 kyr, and may be consistent with a net positive feedback response of the climate–carbon-cycle to elevated volcanic carbon dioxide emissions. Moreover, during the hyperthermal events, different regions may have experienced periods of extreme drought or severe flooding, reflecting the contrasting extremes of climate. Thus, despite differences in nomenclature, these events share a fundamental nature as hyperthermal episodes. These similarities suggest that understanding their commonality might hold essential information on the nature of hyperthermal events and specifically which elements in the climate and carbon cycle contribute to these anomalously warm periods.

Methods

$\delta^{13}C_{org}$ and TOC

Both organic-carbon isotopes ($\delta^{13}C_{org}$) and TOC contents were analysed for a total of 289 samples at the Nanjing Institute of Geology and Palaeontology, Chinese Academy of Sciences. Samples were trimmed to remove visible veins and weathered surfaces and ground using a sample crush (Vibratory Disc Mill RS 200) for geochemical analyses. One gram of homogenised sample was placed in a polypropylene Falcon tube and decarbonated overnight with 3 molar HCl for 24 h. This process was repeated at least three times to ensure the complete removal of carbonates. The carbonate-free residual powder was rinsed 4 times with Milli-Q water to reach neutral pH. Samples were then dried at 60 °C in an oven. Dry samples were crushed, loaded into capsules, and then flash-combusted at 1060 °C in an Organic Elemental Analyser (FLASH, 2000) fitted with a zero blank autosampler. The carbon-isotope composition and TOC content (wt%) of generated CO_2 were measured by a thermal conductivity detector and Delta V Advantage Isotope Ratio Mass Spectrometer, respectively. All isotope data are reported in per mil (‰) variation relative to the Vienna Pee Dee belemnite (VPDB) standard. Calibration of $\delta^{13}C$ values was accomplished using a working standard B2151 ($\delta^{13}C_{org} = -26.27‰$), GBW04407 (black carbon, $\delta^{13}C_{org} = -22.43‰$) and Urea ($\delta^{13}C_{org} = -39.79‰$). The analytical uncertainty for TOC was calculated as a relative error of less than ± 5%, and the standard deviation for $\delta^{13}C_{org}$ was ± 0.2‰ (1σ), both determined through replicate analyses of standard samples.

Mercury concentrations

Hg concentrations were analysed using a Direct Mercury Analyser (DMA80) at the China University of Geosciences (Wuhan). About 150 mg for siltstone/limestone samples and 100 mg for mudstone samples were used in this analysis. Results of low and high Hg were calibrated to the GBW07424 (33 ± 4 ppb Hg) and GBW07403 (590 ± 80 ppb Hg) standards, respectively. One replicate sample and a standard were analysed for every ten samples. Data quality was monitored via multiple analyses of GBW07424 and GBW07403, yielding an analytical precision (2σ) of ± 0.5% of reported Hg concentrations.

Mercury isotopes

Hg isotopes were analyzed at the State Key Laboratory of Environmental Geochemistry, Institute of Geochemistry, Chinese Academy of Sciences, Guiyang. The analysis of Hg-isotopic compositions followed the procedures described in ref.[73]. Hg was extracted and concentrated using the double-combustion and trapping dual-stage protocol[73]. The NIST SRM 997 thallium was used for mass-bias correction, the international Hg standard NIST SRM 3133 was used as an isotopic ref. 73, and the NIST RM 8610 (UM-Almaden Mono-Elemental Secondary Standard) was used as the reference material as a secondary laboratory Hg standard (National Institute of Standards and Technology, Gaithersburg, USA). Procedural blanks were negligible (<0.13 ng, $n = 8$) relative to the amount of Hg in samples (>20 ng). Good recovery (98 ± 4%, 2 SD) guarantees that no Hg-isotope fractionation occurred during the pre-concentration procedure. Volatile ionised Hg^0 generated by $SnCl_2$ reduction in a cold-vapour generation system was introduced into the plasma (Nu-MC–ICP–MS) with Ar as a carrier gas.

Hg-isotopic results are expressed as delta (δ) values in per mil (‰) variation relative to the bracketed NIST 3133 Hg standard, as follows[74]:

$$\delta^{xxx}Hg = [(^{xxx}Hg/^{198}Hg)_{sample}/(^{xxx}Hg/^{198}Hg)_{standard} - 1] \times 1000‰ \quad (1)$$

Any Hg-isotope composition that did not follow the theoretical MDF was considered an isotopic anomaly caused by MIF. MIF values are indicated by capital delta (Δ) notation (in per mil) and predicted from $\delta^{202}Hg$ using the following equations[74]

$$\Delta^{199}Hg = \delta^{199}Hg - 0.252 \times \delta^{202}Hg \quad (2)$$

Reproducibility of $\Delta^{199}Hg$ was better than ± 0.05‰ (2σ).

Elemental analyses

Major and trace elements were analysed for a total of 154 samples at the Nanjing Institute of Geology and Palaeontology, Chinese Academy of Sciences. An ~50 mg of sample powder was weighed and ashed at 110 °C for 3 h. Then, the sample powder was digested in 1 ml of HNO_3 and 1.5 ml of HF at 190 °C for 72 h. After cooling, samples were evaporated at 115 °C to incipient dryness, then 1 mL HNO_3 was added and the sample was dried again. This process was repeated at least three times to ensure the complete removal of HF. The resultant salt was re-dissolved with 1 ml HNO_3 and 2 ml Milli-Q water before it was again sealed and heated in the bomb at 190 °C for 12 h. After completing digestion, these solutions were analyzed for the target elements on a quadrupole inductively coupled plasma mass spectrometer (ICP-MS) and ICP optical emission spectrometer. Two standards (SDO-1, SRM88b) were used to monitor the analytical reproducibility. Precision and accuracy for major and trace elements are estimated to be better than 5% and 1%.

Astronomical cycles

The total 1095 samples for the magnetic susceptibility (MS) experiment were cleaned to remove weathered surfaces and broken into small pieces of ~1–2 mm^3, then filled with 8-cm^3 non-magnetic (plastic) sample boxes. All samples were analyzed on the Kappa Bridge Magnetic Susceptibility System (sensitivity: 3×10^{-8} SI) at the State Key Laboratory of Lake Science and Environment, Nanjing Institute of Geography and Limnology, Chinese Academy of Sciences. Then, all samples were weighed by an electronic balance, with a mass accuracy of 10^{-4} g. The mass magnetic susceptibility (χ) was calculated by the ratio of the measured volume magnetic susceptibility (κ) to rock density. In a relatively humid environment, ferromagnetic minerals such as magnetite and maghaemite imply relatively high MS values, while in a relatively arid environment, carbonate deposits and coarse clastic rocks have relatively low MS values due to the diamagnetism of carbonate and quart[75]. The obtained MS series (χ) were interpolated with a main sampling interval of 0.25 m. To strengthen the orbital signals, we clipped values larger than 8.5×10^{-5} (cm^3/g), and then detrended the series by removing linear trend. We analyzed the periodicity of the untuned and tuned MS series by the Multitaper Method (MTM)[76] and Evolutionary Fast Fourier Transform[77] spectra. The correlation coefficient (COCO) and null hypothesis testing (H0SL)[78] were applied for quantitatively tracking of the sedimentation rates. In the two tuning schemes, the 50–25 m (0.02–0.04 cycles/m) wavelengths filtered via a Gaussian filter and the 16.7–12.5 m (0.06–0.08 cycles/m) wavelengths filtered via a Taner filter are tuned to 405-kyr and 173-kyr synthetically made sinusoids, respectively. The 405-kyr tuning scheme is used to establish a floating astronomical time scale, which is further constrained by the U-Pb age of 232.9 ± 0.7 Ma. The time-height mode is based on the calibration of the peaks of the filtered curve. In the time domain, the long and short eccentricity cycles were filtered by Gaussian (0.0019–0.003 cycles/kyr) and Taner (0.0075–0.0115 cycles/kyr) filters, respectively. The Hilbert transform was used to extract the amplitude modulation of the filtered short eccentricity cycles. The $\delta^{13}C_{org}$ series is calibrated to the time domain based on the 405-kyr tuning scheme with the values below −25.5‰ clipped in order to highlight fluctuations forced by eccentricity, on the scale of ±1‰. Continuous wavelet transform was used to examine the periodicity of the tuned MS series and calibrated $\delta^{13}C_{org}$ series (values clipped below −25.5‰). The proportion of hygrophyte was calibrated to the time domain based on the age model of the established ATS. All of the time-series analyses were conducted using Acycle 2.8[79].

Model simulations

To examine the spatio-temporal changes in temperature and precipitation during the CPE, we performed climate simulations using AWI-ESM[80]. AWI-ESM is a coupled ocean-atmosphere model widely used in palaeoclimate research. The land-sea distribution and topography is applied from the reconstructed palaeo-digital elevation model[41] from 235 million years ago. There is no continental ice sheet. The ocean component of AWI-ESM employed an unstructured triangle mesh with horizontal resolution ranging from 30 ~ 270 kilometres (Supplementary Fig. 18), whereas the atmosphere component used a consistent horizontal resolution of 3.75° × 3.75°. We performed climate simulations under different atmospheric CO_2 levels, i.e., 568, 1136, 1704, and 2272 ppmv. At the end, the 568 ppmv experiment is used as an analogue of the climate prior to the CPE, while the 1704 ppmv experiment is used to mimic the relatively warmer climate during the CPE. Two criteria were used in the selection process: first, the selected CO_2 levels are close to the proxy-based reconstruction of atmospheric CO_2 before and during the CPE[81]; second, the simulated global mean surface temperatures are close to those previously reconstructed[1,41]. A similar approach was also applied in previous studies to reconstruct the deep-time Earth's climate[71,82]. It should be noted that the simulated climate change patterns in greenhouse climates do not differ much depending on the CO_2 level. Differences in CO_2 levels primarily affect the amplitude of climate changes. All other boundary conditions, such as solar constant and Earth's orbit, were kept the same as the pre-industrial era, unless specifically stated. The 568 ppmv experiment was run for 2000 years to allow the climate system to reach a surface equilibrium state. The 1704 ppmv experiment, initialised from the first experiment, was run for 1000 years. This procedure allows the upper ocean and surface climate to achieve an equilibrium state. The last 100 years of the two experiments were used for comparison.

Data availability

The scientific data generated in this study are provided in the Supplementary Data file.

References

1. Judd, E. J. et al. A 485-million-year history of Earth's surface temperature. *Science* **385**, eadk3705 (2024).
2. Marshall, M. A. Million years of Triassic rain. *Nature* **576**, 26–28 (2019).
3. Dal Corso, J. et al. Extinction and dawn of the modern world in the Carnian (Late Triassic). *Sci. Adv.* **6**, eaba0099 (2020).
4. Tomimatsu, Y. et al. Pelagic responses to oceanic anoxia during the Carnian pluvial episode (Late Triassic) in Panthalassa Ocean. *Sci. Rep.* **13**, 16316 (2023).
5. Lin, F. et al. Deoxygenation preceding the Carnian Pluvial episode (Late Triassic) in the Qiangtang Basin (Tibetan Plateau): implications for organic and inorganic geochemistry and petrography. *Mar. Pet. Geol.* **173**, 107289 (2025).
6. Roghi, G., Gianolla, P., Minarelli, L., Pilati, C. & Preto, N. Palynological correlation of Carnian humid pulses throughout western Tethys. *Palaeogeogr. Palaeoclimatol. Palaeoecol.* **290**, 89–106 (2010).
7. Mueller, S., Krystyn, L. & Kürschner, W. M. Climate variability during the Carnian Pluvial Phase—a quantitative palynological study of the Carnian sedimentary succession at Lunz am See, Northern Calcareous Alps, Austria. *Palaeogeogr. Palaeoclimatol. Palaeoecol.* **441**, 198–211 (2016).
8. Baranyi, V., Rostási, Á., Raucsik, B. & Kürschner, W. M. Palynology and weathering proxies reveal climatic fluctuations during the Carnian Pluvial Episode (CPE) (Late Triassic) from marine successions in the Transdanubian Range (western Hungary). *Glob. Planet. Change* **177**, 157–172 (2019).
9. Zhang, P. et al. Four volcanically driven climatic perturbations led to enhanced continental weathering during the late Triassic Carnian Pluvial Episode. *Earth Planet. Sci. Lett.* **626**, 118517 (2024).
10. Simms, M. J. & Ruffell, A. H. Synchroneity of climatic change and extinctions in the Late Triassic. *Geology* **17**, 265–268 (1989).
11. Sun, Y. D. et al. Climate warming, euxinia and carbon isotope perturbations during the Carnian (Triassic) crisis in South China. *Earth Planet. Sci. Lett.* **444**, 88–100 (2016).

12. Li, Z. H., Chen, Z. Q., Zhang, F. F., Ogg, J. G. & Zhao, L. S. Global carbon cycle perturbations triggered by volatile volcanism and ecosystem responses during the Carnian Pluvial Episode (Late Triassic). *Earth Sci. Rev.* **211**, 103404 (2020).
13. Bernardi, M., Gianolla, P., Petti, F. M., Mietto, P. & Benton, M. J. Dinosaur diversification linked with the Carnian Pluvial Episode. *Nat. Commun.* **9**, 1499 (2018).
14. Müller, R. T. & Garcia, M. S. A new silesaurid from Carnian beds of Brazil fills a gap in the radiation of avian line archosaurs. *Sci. Rep.* **13**, 4981 (2023).
15. Reolid, M. et al. Ichnological evidence of semi-aquatic locomotion in early turtles from eastern Iberia during the Carnian Humid Episode (Late Triassic). *Palaeogeogr. Palaeoclimatol. Palaeoecol.* **490**, 450–461 (2018).
16. Irmis, R. B., Nesbitt, S. J. & Sues, H. D. Early crocodylomorpha. *Geol. Soc. Spec. Publ.* **379**, 275–302 (2013).
17. Kustatscher, E. et al. *Flora of the Late Triassic*. In *The Late Triassic World* (eds Tanner, L.) 545–622 (Springer Cham, 2018).
18. Seyfullah, L. J., Roghi, G., Corso, J. D. & Schmidt, A. R. The Carnian Pluvial Episode and the first global appearance of amber. *J. Geol. Soc. Lond.* **175**, 1012–1018 (2018).
19. Dal Corso, J. et al. Discovery of a major negative ^{13}C spike in the Carnian (Late Triassic) linked to the eruption of Wrangellia flood basalts. *Geology* **40**, 79–82 (2012).
20. Dal Corso, J. et al. Multiple negative carbon-isotope excursions during the Carnian Pluvial Episode (Late Triassic). *Earth Sci. Rev.* **185**, 732–750 (2018).
21. Muttoni, G. et al. A middle-late triassic (Ladinian-Rhaetian) carbon and oxygen isotope record from the Tethyan Ocean. *Palaeogeogr. Palaeoclimatol. Palaeoecol.* **399**, 246–259 (2014).
22. Mueller, S., Hounslow, M. W. & Kürschner, W. M. Integrated stratigraphy and palaeoclimate history of the Carnian Pluvial Event in the Boreal realm: new data from the Upper Triassic Kapp Toscana Group in central Spitsbergen (Norway). *J. Geol. Soc. Lond.* **173**, 186–202 (2016).
23. Sun, Y. D., Richoz, S., Krystyn, L., Zhang, Z. T. & Joachimski, M. M. Perturbations in the carbon cycle during the Carnian humid episode: Carbonate carbon isotope records from southwestern China and northern Oman. *J. Geol. Soc. Lond.* **176**, 167–177 (2019).
24. Miller, C. S. et al. Astronomical age constraints and extinction mechanisms of the Late Triassic Carnian crisis. *Sci. Rep.* **7**, 2557 (2017).
25. Furin, S. et al. High-precision U-Pb zircon age from the Triassic of Italy: implications for the Triassic time scale and the Carnian origin of calcareous nannoplankton and dinosaurs. *Geology* **34**, 1009–1012 (2006).
26. Lu, J. et al. Volcanically driven lacustrine ecosystem changes during the Carnian Pluvial Episode (Late Triassic). *Proc. Natl Acad. Sci. Usa.* **118**, e2109895118 (2021).
27. Mazaheri-Johari, M. et al. Mercury deposition in Western Tethys during the Carnian Pluvial Episode (Late Triassic). *Sci. Rep.* **11**, 17339 (2021).
28. Tomimatsu, Y. et al. Marine osmium isotope record during the Carnian "pluvial episode" (Late Triassic) in the pelagic Panthalassa Ocean. *Glob. Planet. Change* **197**, 103387 (2021).
29. Zhao, H. et al. Mercury enrichments during the Carnian pluvial event (Late Triassic) in South China. *Geol. Soc. Am. Bull.* **134**, 2709–2720 (2022).
30. Jin, X. et al. Climax in Wrangellia LIP activity coincident with major Middle Carnian (Late Triassic) climate and biotic changes: mercury isotope evidence from the Panthalassa pelagic domain. *Earth Planet. Sci. Lett.* **607**, 118075 (2023).
31. Zhang, Q. et al. Orbitally-paced climate change during the Carnian Pluvial Episode. *Earth Planet. Sci. Lett.* **626**, 118546 (2024).
32. Dal Corso, J., Mills, B. J., Chu, D., Newton, R. J. & Song, H. Background Earth system state amplified Carnian (Late Triassic) environmental changes. *Earth Planet. Sci. Lett.* **578**, 117321 (2022).
33. Coram, R. A. & Radley, J. D. The Carnian pluvial episode: a damp squib for life on land?. *Proc. Geol. Assoc.* **134**, 551–561 (2023).
34. Zhao, X. D., Xue, N. H., Peng, J. G., Zhang, H. C. & Wang, B. Terrestrial responses to the Carnian Pluvial Episode in the Late Triassic: Research status and prospects. *Quat. Sci.* **44**, 1127–1140 (2024).
35. Olsen, P. E. & Kent, D. V. High-resolution early Mesozoic Pangean climatic transect in lacustrine environments. In *Epicontinental Triassic* (eds Bachman, G. & Lerche I.) 1475–1496 (Schweizerbart Science Publishers Stuttgart, 2000).
36. Baranyi, V., Miller, C. S., Ruffell, A., Hounslow, M. W. & Kürschner, W. M. A continental record of the Carnian Pluvial Episode (CPE) from the Mercia Mudstone Group (UK): palynology and climatic implications. *J. Geol. Soc. Lond.* **176**, 149–166 (2019).
37. Franz, M., Kustatscher, E., Heunisch, C., Niegel, S. & Röhling, H. G. The Schilfsandstein and its flora; arguments for a humid mid-Carnian episode?. *J. Geol. Soc. Lond.* **176**, 133–148 (2019).
38. Fijałkowska-Mader, A., Jewuła, K. & Bodor, E. Record of the Carnian Pluvial Episode in the Polish microflora. *Palaeoworld* **30**, 106–125 (2021).
39. Cho, T., Ikeda, M. & Ohta, T. Increased terrigenous supply to the pelagic Panthalassa superocean across the Carnian pluvial episode: a possible link with extensive aridification in the Pangaea interior. *Front. Earth Sci.* **10**, 897396 (2022).
40. Grasby, S. E., Them, T. R., Chen, Z. H., Yin, R. S. & Ardakani, O. H. Mercury as a proxy for volcanic emissions in the geologic record. *Earth Sci. Rev.* **196**, 102880 (2019).
41. Scotese, C. R. An atlas of Phanerozoic paleogeographic maps: the seas come in and the seas go out. *Annu. Rev. Earth Planet. Sci.* **49**, 679–728 (2021).
42. Peng, J., Slater, S. M. & Vajda, V. Floral and faunal biostratigraphy of the middle–upper Triassic Karamay and Huangshanjie formations from the southern Junggar Basin, China. *Geol. Soc. Spec. Publ.* **538**, 41–66 (2024).
43. Ogg, J. G. Triassic (chapter 25). In *The Geologic Time Scale 2012* (eds Gradstein, F. M., Ogg, J. G., Schmitz, M. D., Ogg, G. M.) (Elsevier, Amsterdam, 2012).
44. Laskar, J. et al. A long-term numerical solution for the insolation quantities of the Earth. *Astron. Astrophys.* **428**, 261–285 (2004).
45. Laskar, J. Astrochronology. In *Geologic Time Scale 2020* (eds Gradstein, F. M., Ogg, J. G., Schmitz, M. B. & Ogg, G. M.) 139–158 (Elsevier Amsterdam, 2020).
46. Bowen, G. J. et al. Two massive, rapid releases of carbon during the onset of the Palaeocene–Eocene thermal maximum. *Nat. Geosci.* **8**, 44–47 (2015).
47. Ruhl, M. et al. On the onset of Central Atlantic Magmatic Province (CAMP) volcanism and environmental and carbon-cycle change at the Triassic–Jurassic transition (Neuquén Basin, Argentina). *Earth Sci. Rev.* **208**, 103229 (2020).
48. Yao, H. et al. Mercury evidence of intense volcanism preceded Oceanic anoxic event 1d. *Geophys. Res. Lett.* **48**, e2020GL091508 (2021).
49. Kuhnt, W. et al. Unravelling the onset of Cretaceous Oceanic Anoxic Event 2 in an extended sediment archive from the Tarfaya-Laayoune Basin, Morocco. *Paleoceanogr* **32**, 923–946 (2017).
50. Babila, T. L. et al. Surface ocean warming and acidification driven by rapid carbon release precedes Paleocene-Eocene Thermal Maximum. *Sci. Adv.* **8**, eabg1025 (2022).
51. Dal Corso, J., Sun, Y. & Kemp, D. B. Palaeogeographic heterogeneity of large-amplitude changes in marine sedimentation rates during the Carnian Pluvial Episode (Late Triassic). *Glob. Planet. Change* **237**, 104437 (2024).

52. Shen, J., Yin, R., Algeo, T. J., Svensen, H. H. & Schoepfer, S. D. Mercury evidence for combustion of organic-rich sediments during the end-Triassic crisis. *Nat. Commun.* **13**, 1307 (2022).
53. Nozaki, O. et al. 2019, Triassic marine Os isotope record from a pelagic chert succession, Sakahogi section, Mino Belt, southwest Japan. *J. Asian Earth Sci.: X* **1**, 100004 (2019).
54. Kender, S. et al. Paleocene/Eocene carbon feedbacks triggered by volcanic activity. *Nat. Commun.* **12**, 5186 (2021).
55. Zeebe, R. E., Ridgwell, A. & Zachos, J. C. Anthropogenic carbon release rate unprecedented during the past 66 million years. *Nat. Geosci.* **9**, 325–329 (2016).
56. Sun, Y. et al. Mega El Niño instigated the end-Permian mass extinction. *Science* **385**, 1189–1195 (2024).
57. Kemp, D. B. et al. The timing and duration of large-scale carbon release in the Early Jurassic. *Geology* **52**, 891–895 (2024).
58. Bauer, K. W. et al. A climate threshold for ocean deoxygenation during the Early Cretaceous. *Nature* **633**, 582–586 (2024).
59. Scotese, C. R., Song, H., Mills, B. J. & van der Meer, D. G. Phanerozoic paleotemperatures: The earth's changing climate during the last 540 million years. *Earth Sci. Rev.* **215**, 103503 (2021).
60. Biskaborn, B. K. et al. Permafrost is warming at a global scale. *Nat. Commun.* **10**, 264 (2019).
61. Gornitz, V. & Fung, I. Potential distribution of methane hydrates in the world's oceans. *Glob. Biogeochem. Cycles* **8**, 335–347 (1994).
62. Huang, H. et al. Organic carbon burial is paced by a ~173-ka obliquity cycle in the middle to high latitudes. *Sci. Adv.* **7**, eabf9489 (2021).
63. De Vleeschouwer, D. et al. High-latitude biomes and rock weathering mediate climate–carbon cycle feedbacks on eccentricity timescales. *Nat. Commun.* **11**, 5013 (2020).
64. Martinez, M. & Dera, G. Orbital pacing of carbon fluxes by a ~9-My eccentricity cycle during the Mesozoic. *Proc. Natl Acad. Sci. Usa.* **112**, 12604–12609 (2015).
65. Storm, M. S. et al. Orbital pacing and secular evolution of the Early Jurassic carbon cycle. *Proc. Natl Acad. Sci. Usa.* **117**, 3974–3982 (2020).
66. Klausen, T. G., Nyberg, B. & Helland-Hansen, W. The largest delta plain in Earth's history. *Geology* **47**, 470–474 (2019).
67. Hornung, T., Brandner, R., Krystyn, L., Joachimski, M. M. & Keim, L. Multistratigraphic constraints on the NW Tethyan "Carnian crisis". *N. Mex. Mus. Nat. Hist. Sci. Bull.* **41**, 59–67 (2007).
68. Rostási, Á., Raucsik, B. & Varga, A. Palaeoenvironmental controls on the clay mineralogy of Carnian sections from the Transdanubian Range (Hungary). *Palaeogeogr. Palaeoclimatol. Palaeoecol.* **300**, 101–112 (2011).
69. Shi, Z. et al. The Carnian pluvial episode at Ma'antang, Jiangyou in upper Yangtze block, Southwestern China. *J. Geol. Soc. Lond.* **176**, 197–207 (2019).
70. Landwehrs, J. et al. Modes of Pangean lake level cyclicity driven by astronomical climate pacing modulated by continental position and pCO_2. *Proc. Natl Acad. Sci. USA.* **119**, e2203818119 (2022).
71. Li, X. et al. A high-resolution climate simulation dataset for the past 540 million years. *Sci. Data* **9**, 371 (2022).
72. Cramwinckel, M. J. et al. Global and zonal-mean hydrological response to early Eocene warmth. *Paleoceanogr. Paleoclimatol.* **38**, e2022PA004542 (2023).
73. Fu, X. et al. Significant seasonal variations in isotopic composition of atmospheric total gaseous mercury at forest sites in China caused by vegetation and mercury sources. *Environ. Sci. Technol.* **53**, 13748–13756 (2019).
74. Blum, J. D. & Bergquist, B. A. Reporting of variations in the natural isotopic composition of mercury. *Anal. Bioanal. Chem.* **388**, 353–359 (2007).
75. Boulila, S. et al. Milankovitch and sub-milankovitch forcing of the oxfordian (Late Jurassic) terres noires formation (SE France) and global implications. *Basin Res* **22**, 717–732 (2010).
76. Thomson, D. J. Spectrum estimation and harmonic analysis. *Proc. IEEE* **70**, 1055–1096 (1982).
77. Kodama, K. P. Hinnov, L. A. *Rock Magnetic Cyclostratigraphy*, 176 (Wiley-Blackwell 2014).
78. Li, M., Kump, L. R., Hinnov, L. A. & Mann, M. E. Tracking variable sedimentation rates and astronomical forcing in Phanerozoic paleoclimate proxy series with evolutionary correlation coefficients and hypothesis testing. *Earth Planet. Sci. Lett.* **501**, 165–179 (2018).
79. Li, M., Hinnov, L. & Kump, L. Acycle: time-series analysis software for paleoclimate research and education. *Comput. Geosci.* **127**, 12–22 (2019).
80. Sidorenko, D. et al. Evaluation of FESOM2.0 coupled to ECHAM6.3: preindustrial and HighResMIP simulations. *J. Adv. Model. Earth Syst.* **11**, 3794–3815 (2019).
81. Foster, G. L., Royer, D. L. & Lunt, D. J. Future climate forcing potentially without precedent in the last 420 million years. *Nat. Commun.* **8**, 14845 (2017).
82. Li, X. et al. Climate variations in the past 250 million years and contributing factors. *Paleoceanogr. Paleoclimatol.* **38**, e2022PA004503 (2023).

Acknowledgements

We are grateful to P.E. Olsen and M. Li for helpful discussions; X. Zhang, H. Sun and L. Li for their help in the fieldtrip; C. Guan, J. Shen, M. Lv, and G. Li for their assistance with the lab works; D. Yang for the artistic reconstruction. This work was supported by the National Natural Science Foundation of China (42125201 and 42293280 to B.W., 42402012 to X.Z., 42311530682 to P.C., 42402030 to M.W.) and the Youth Innovation Promotion Association of the Chinese Academy of Sciences (2022310 to S.L.).

Author contributions

B.W. conceived the project. X.Z., N.X., H.Y., D.Z., J.P., Y.F., S.L., J.S., H.Z. and B.W. conducted the fieldwork and collected the samples. X.Z., B.W., J.F., Y.F., S.L., X.F., W.J., X.Z., H.C.J. and P.C. prepared and performed the geochemical analyses. N.X., D.D.V., B.W., Y.F., and M.W. designed and analysed the astronomical cycles work. H.Y. and Q.W. contributed their expertise in Earth system modelling, while N.X. and X.Z. provided valuable data and information. D.Z., H.Z. and J.S. performed the U-Pb dating analyses. J.P. and X.Z. conducted palynological analyses. All the authors contributed to the data interpretation. X.Z., N.X., H. Y. and B.W. wrote the manuscript, with comments from all authors. All authors discussed the results and approved the final manuscript.

Competing interests

The authors declare no competing interests.

Additional information

Supplementary information The online version contains supplementary material available at https://doi.org/10.1038/s41467-025-61262-7.

Correspondence and requests for materials should be addressed to Bo Wang.

Peer review information *Nature Communications* thanks Yadong Sun and the other, anonymous, reviewers for their contribution to the peer review of this work. A peer review file is available.

https://doi.org/10.1038/s41467-025-61262-7